Research article

Fei Ding*, Yiting Chen and Sergey I. Bozhevolnyi

Focused vortex-beam generation using gap-surface plasmon metasurfaces

https://doi.org/10.1515/nanoph-2019-0235
Received August 3, 2019; revised October 14, 2019; accepted October 20, 2019

Abstract: In spite of a wide range of applications ranging from particle trapping to optical communication, conventional methods to generate vortex beams suffer from bulky configurations and limited performance. Here, we design, fabricate, and experimentally demonstrate orthogonal linear-polarization conversion and focused vortex-beam generation simultaneously by using gap-surface plasmon metasurfaces that enable high-performance linear-polarization conversion along with the complete phase control over reflected fields, reproducing thereby the combined functionalities of traditional half-wave plates, lenses, and q-plates. The fabricated metasurface sample features the excellent capability of orthogonal linear-polarization conversion and focused vortex-beam generation within the wavelength range of 800–950 nm with an averaged polarization conversion ratio of ~80% and absolute focusing efficiency exceeding 27% under normal illumination with the *x*-polarized beam. We further show that this approach can be extended to realize a dual-focal metasurface with distinctly engineered intensity profiles by using segmented metasurfaces, where an orthogonal-polarized beam with Gaussian-distributed intensity and a vortex beam with intensity singularity have been experimentally implemented. The proposed multifunctional metasurfaces pave the way for advanced research and applications targeting photonics integration of diversified functionalities.

Keywords: linear-polarization conversion; focused vortex-beam; gap-surface plasmon metasurface.

1 Introduction

The optical vortex beam with phase singularity was first discovered in the 1990s, which possesses a helical phase front so that the Poynting vector within the beam is twisted with respect to the principal axis of light propagation [1]. In contrast to the spin angular momentum that can take only two values, the orbital angular momentum carried by the vortex beam is unbounded since the topological charge l can take an arbitrary value within a continuous range. Therefore, vortex beams are being considered as potential candidates for encoding information in optical communication, which can greatly increase the information capacity [2, 3]. Besides optical communication, vortex beams can also be used in particle trapping [4] and quantum systems [5]. Conventional methods, including q-plates and spatial light modulator, have been widely used to generate vortex beams. However, these systems are intrinsically bulky and could not be straightforwardly minimized and integrated, preventing from widespread applications in nanophotonics. In addition, these ordinary vortex-beam generators are only designed for creating vortex beams with planar output wavefronts. If a focused vortex beam is required, additional lenses or parabolic reflectors need to be added into the optical path, resulting in complicated optical systems. In this regard, there are numerous challenges in building compact and ultrathin optical devices capable of generating focused vortex beams.

In recent years, optical metasurfaces, planar artificial materials with surface-confined configurations, have attracted progressively increasing attention and started to revolutionize optical designs by replacing traditional bulky optical components with meta-devices that exhibit the advantages of planar profiles, compactness, and low cost [6–10]. Due to the unprecedented capabilities of directly modifying the boundary conditions for impinging optical waves by arranging meta-atoms with tailored optical responses, metasurfaces have also been explored to generate vortex beams [11–16]. Despite certain achievements, the aforementioned metasurface-based vortex-beam generators just produce vortex beams with planar wavefronts, restricting severely the range of practical

***Corresponding author: Fei Ding,** SDU Nano Optics, University of Southern Denmark, Campusvej 55, DK-5230 Odense, Denmark, e-mail: feid@mci.sdu.dk. https://orcid.org/0000-0001-7362-519X
Yiting Chen and Sergey I. Bozhevolnyi: SDU Nano Optics, University of Southern Denmark, Campusvej 55, DK-5230 Odense, Denmark. https://orcid.org/0000-0002-4003-4796 (Y. Chen); https://orcid.org/0000-0002-0393-4859 (S.I. Bozhevolnyi)

applications. In particular, it is highly desired to efficiently integrate multiple diversified functionalities into a single design and supply additional degrees of freedom to control the wavefronts (i.e. phase and polarization) of the output vortex beams while maintaining the advantages of planar profiles, compactness, and relative ease of fabrication [17–22].

In this paper, we combine the functionalities of conventional half-wave plates (HWPs), lenses, and q-plates into single meta-devices to experimentally realize gap-surface plasmon (GSP) metasurfaces for simultaneous orthogonal linear-polarization conversion and focused vortex-beam generation under the excitation of a linearly polarized light. The fabricated metasurfaces exhibit excellent capability of linear-polarization conversion (>80% on average) and focusing (absolute average efficiency >27%) within the wavelength range of 800–950 nm. Furthermore, a dual-focal metasurface is experimentally demonstrated to focus the incident light into two spots with distinctly engineered wavefronts at different locations in the same focal plane, indicating the potential for generating spatially multiplexed meta-devices.

2 Results and discussions

Figure 1A schematically illustrates the working principle of the proposed GSP metasurface for orthogonal linear-polarization conversion and focused vortex-beam generation. Once an *x*-polarized beam is incident on the metasurface at normal incidence, the reflected waves will become cross-polarized (i.e. *y*-polarized), gain additional phase shifts, and then interfere constructively in the far field, thereby forming a focused vortex beam in cross-polarization. Specifically, the basic GSP meta-atom consists of gold (Au) nanoantennas tilted by 45° with respect to the *x*-axis, a middle silicon dioxide (SiO_2) spacer layer, and a bottom continuous Au film, which functions as a nanoscale HWP (nano-HWP) to, simultaneously and independently, engineer the phase and polarization of the reflected light (Figure 1B) [23]. When an *x*-polarized wave is normally impinging on the meta-atoms, electric-dipole oscillations along the long and short axis of the Au nanoantennas are excited, resulting in the cross-polarized scattering. The cross-polarized scattering is further enhanced by the constructive interference in the multireflection process within the GSP cavity, consequently leading to highly efficient orthogonal linear-polarization conversion [24–26].

The design principle of such a GSP metasurface is based on the use of meta-atoms that enable the HWP functionality, i.e. efficient orthogonal linear-polarization conversion, along with the complete phase control over the polarization-converted reflected fields. Taking into account the fact that the phase of the reflected cross-polarized field can be changed by π radian simply by rotating the corresponding meta-atom over 90°, designing two meta-atoms that produce the reflected cross-polarized fields with the phases φ_{cr1} and φ_{cr2} being different by $\pi/2$ (elements 1 and 2 in Figure 2A) is sufficient to construct the four-element-based phase gradient metasurface

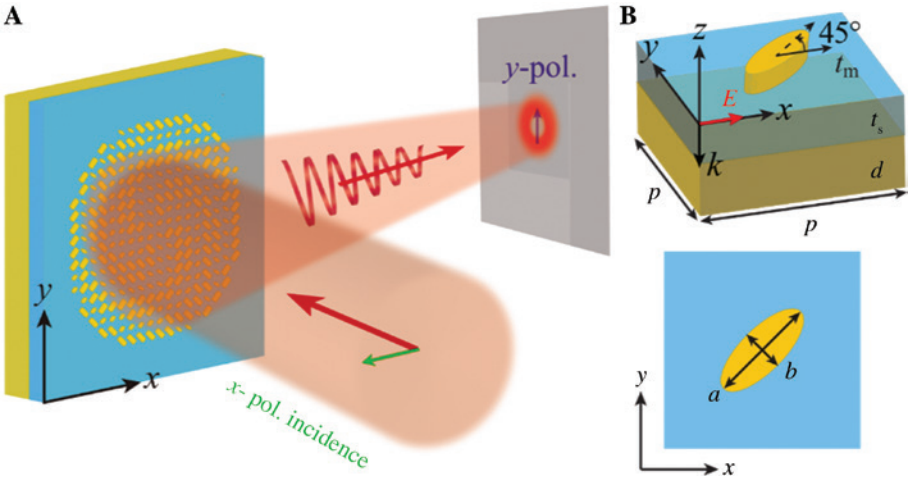

Figure 1: Schematic of the metasurface.
(A) Artistic illustration of the metasurface for linear-polarization conversion and focused vortex-beam generation. (B) Schematic of the basic meta-atom that consists of an Au nanoantenna on top of a spacer and Au substrate with dimensions of $p = 550$ nm, $d = 130$ nm, $t_s = 110$ nm, and $t_m = 80$ nm.

by rotating elements 1 and 2 over 90° so as to cover the whole 2π range, because $\varphi_{cr3}=\varphi_{cr1}+\pi$ and $\varphi_{cr4}=\varphi_{cr2}+\pi$. By tailoring the shapes and dimensions (a and b) of the topmost Au nanoantennas, we can independently control the reflection phase of the cross-polarized reflected light, achieving eventually the desired phase relationship $\varphi_{cr2}=\varphi_{cr1}+\pi/2$ at the design wavelength of $\lambda_d=850$ nm and enabling the design of the four-element supercell

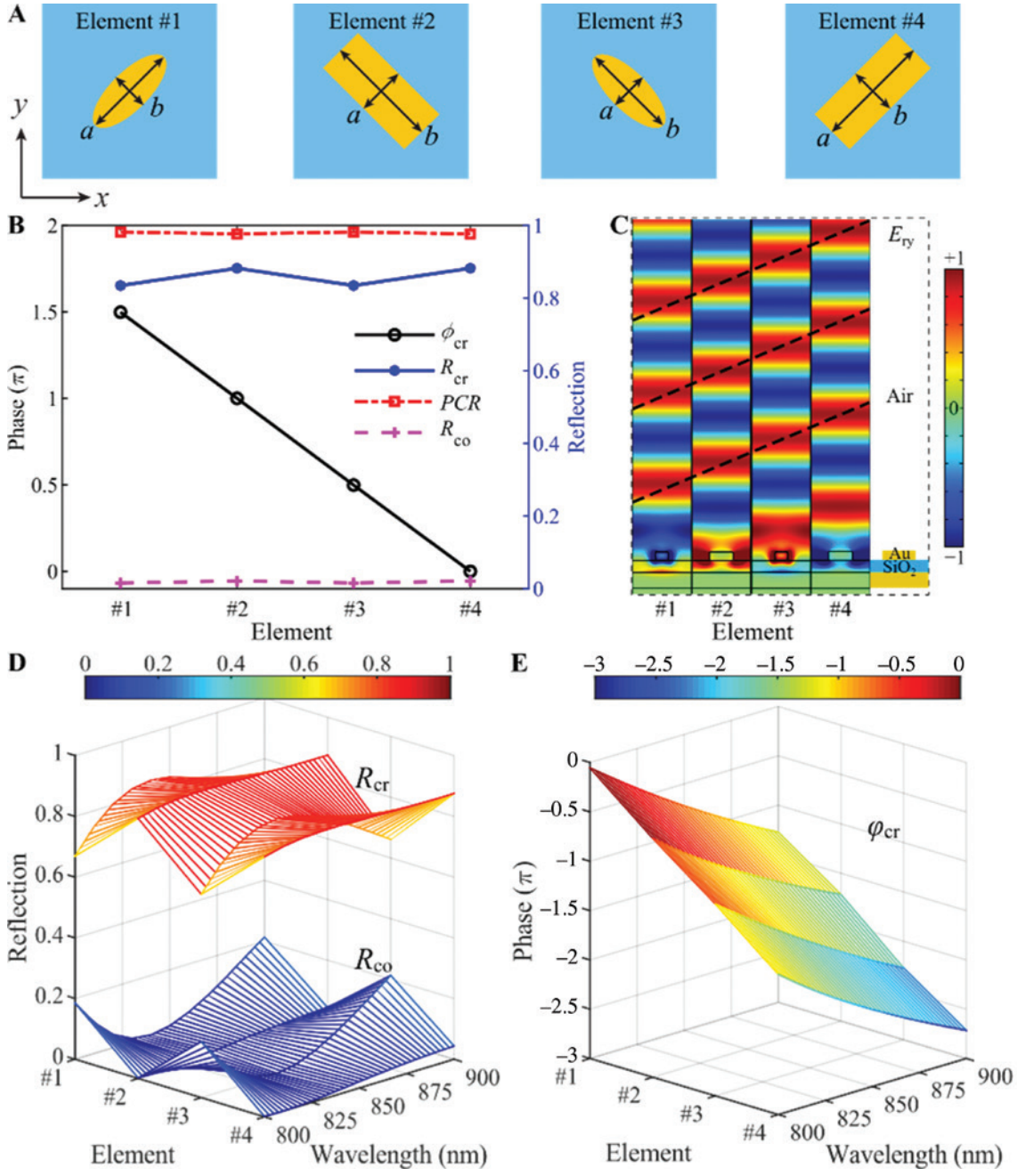

Figure 2: Reflection amplitude and phase responses of the selected meta-atoms.
(A) Schematic of the four meta-atoms. The dimensions of element 1–4 are (1) $a=228$ nm, $b=90$ nm; (2) $a=155$ nm, $b=360$ nm; (3) $a=90$ nm, $b=228$ nm; (4) $a=360$ nm, $b=155$ nm, indicating that elements 3 and 4 are simply rotated by 90° with respect to elements 1 and 2, respectively. (B) Simulated cross-polarized reflection phase φ_{cr}, cross-polarized reflectivity R_{cr}, co-polarized reflectivity R_{co}, and linear-polarization conversion ratio *PCR* of the four elements at $\lambda_d=850$ nm. (C) Simulated electric field distribution (E_y) in each meta-atom at $\lambda_d=850$ nm when an x-polarized plane wave is incident from the top. (D, E) Simulated cross-polarized reflectivity R_{cr}, co-polarized reflectivity R_{co}, and cross-polarized reflection phase φ_{cr}, respectively, for four meta-atoms as a function of incident wavelength.

(the details of simulation is shown in Supplementary Section S1). The simulated cross-polarized reflectivity R_{cr}, co-polarized reflectivity R_{co}, orthogonal linear-polarization conversion ratio PCR [$PCR = R_{cr}/(R_{cr}+R_{co})$], and cross-polarized reflection phase φ_{cr} of the four selected meta-atoms indicate that each of the four meta-atoms functions as a reflective nano-HWP with high efficiency at $\lambda_d = 850$ nm (Figure 2B). Specifically, the linear-polarization conversion efficiency is over 95% with the averaged cross-polarized reflectivity of ~85%. At the same time, a linear phase gradient with the phase increment of π/2 between adjacent meta-atoms has been realized for the cross-polarized reflected light. When the field distributions of the four meta-atoms are plotted side by side, one can see that the wavefronts of the cross-polarized reflected light experience significantly different phase shifts upon interaction with the meta-atoms, forming four phase values with the phase step of π/2 (Figure 2C). Consequently, the cross-polarized reflected light would be steered into the perpendicular direction to the titled wavefronts marked with the black dashed line. As a final comment, it should be noted that the designed metasurfaces maintain high-efficiency linear-polarization conversion over a broad wavelength range of 800–900 nm as the phase gradient for all four meta-atoms remains approximately linear, thus enabling the broadband manipulation of the cross-polarized reflected light (Figure 2D and E).

To generate a focused vortex beam with orthogonal linear-polarization conversion, the GSP metasurface should first incorporate the phase profiles of a lens and a q-plate together. Therefore, the phase distribution imposed on the metasurface is calculated via the following formula:

$$\varphi(x, y) = \frac{2\pi}{\lambda_d}\left(\sqrt{x^2+y^2+f^2} - f\right) + l \cdot \arctan\left(\frac{y}{x}\right) \quad (1)$$

where λ_d is the design wavelength in free space, f is the focal length, and l is the topological charge. Figure 3A displays the phase profile of the designed focused vortex-beam generator with a diameter of $D = 50$ μm, a focal length of $f = 60$ μm, and the topological charge of $l = 2$, indicating the twofold spiral distribution. The phase profile is then discretized in steps on the x–y plane and implemented using the meta-atoms (Figure 3B). Within the metasurface, all meta-atoms are rotated by 45° with respect to the x-axis, ensuring that the x-polarized incident light is efficiently converted into the cross-polarized reflected beam. Figure 3C presents the scanning electron microscope (SEM) images of the sample fabricated with standard electron-beam lithography (Supplementary Section S2), displaying the twofold spiral pattern consistent with the twofold spiral phase distribution. Following the fabrication, we characterized the metasurface sample

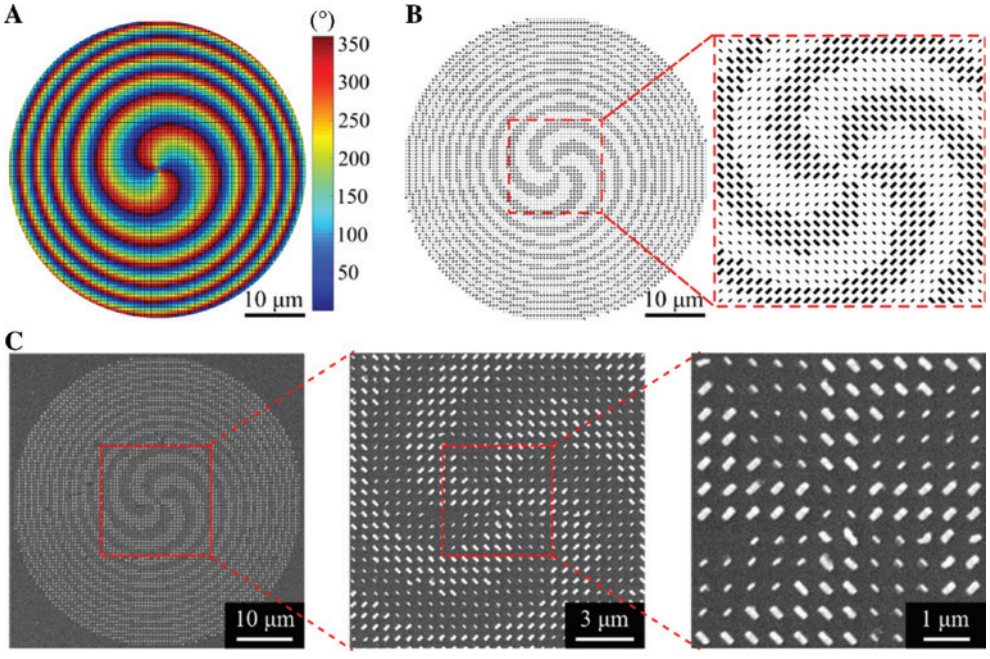

Figure 3: Design and fabrication of the focused vortex-beam generator with a diameter of $D = 50$ μm, a focal length of $f = 60$ μm, and the topological charge of $l = 2$ at $\lambda_d = 850$ nm.
(A, B) Calculate phase profile and designed geometry of the metasurface. (C) SEM images of the fabricated sample.

using a home-built optical system that includes a couple of optical components mounted on a three-dimensional translation stage (Supplementary Section S3). By moving all the mounted components together along the axis of light propagation (z-direction) step by step, we could record the intensity profiles at different x–y planes in sequence and reconstruct the three-dimensional intensity distribution.

We plot in Figure 4A–C the measured cross-polarized intensity distributions at different wavelengths when the fabricated sample is illuminated with an x-polarized Gaussian beam at normal incidence. As shown in the left panels of Figure 4A–C, the two-dimensional intensity slices along the z-direction reveal the evolution of the generated vortex beam, which is slightly focused at the corresponding focal plane of each wavelength. All the intensity patterns on the x–y planes have the doughnut-shaped intensity distributions with the intensity minimum at the center, which is the main characteristic of the vortex beams, that is, intensity singularity. To prove the helicity wavefront of the focused vortex beam, we performed the interference experiment by using a home-built Michelson interferometer, where the generated vortex beam and the tilted Gaussian beam are arranged in the sample and reference arms, respectively (Supplementary Figure S2). The fork dislocations are observable in the interference patterns (Figure 4A–C), verifying the phase singularity in a broadband spectrum. If the topological charge l is increased from 1 to 3, the corresponding focal spot expands, and the ring radius of the vortex intensity profile becomes larger accordingly, while the doughnut shape is preserved (Supplementary Figure S3). Additionally, the number of dislocations would be equal to the increased topological charge.

Since the focused vortex beam is solely assembled by the cross-polarized light, *PCR* can quantitatively

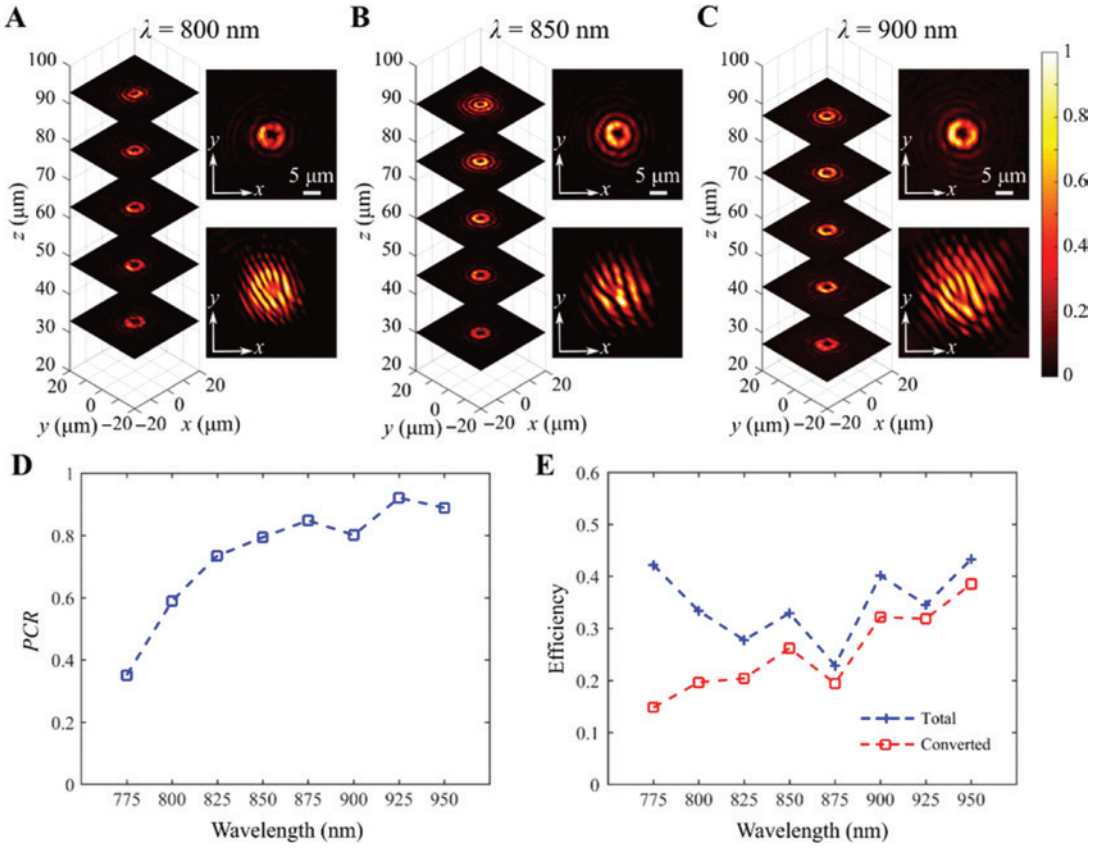

Figure 4: Optical characterization of the fabricated vortex-beam generator with the topological charge of $l = 2$.
Left (A–C): focal spots evolution of the generated vortex beam along the optical axis (z-axis) in cross-polarization. Right top (A–C): measured focal spot profiles at the corresponding focal planes in cross-polarization. Right down (A–C): interference pattern of the focused vortex beam and the copropagating Gaussian beam when the beam axes are tilted with respect to the other. (D) Measured *PCR* as a function of wavelength. (E) Measured efficiency as a function of wavelength. The total efficiency is defined as the ratio of the light intensity from the corresponding focal spot to the incident intensity, while the converted efficiency only considers the cross-polarized reflected beam. In all measurement, the x-polarized Gaussian beam is normally incident on the sample.

gauge the conversion efficiency of the metasurface, which is defined as the ratio of the power within the vortex beam in cross-polarization to the overall reflected power [13]. As depicted in Figure 4D, the fabricated sample exhibits efficient ($PCR > 80\%$ on average) focused vortex-beam generation in a wide wavelength spectrum ranging from 800 to 950 nm, superior to some of the reported vortex-beam generators based on plasmonic metasurfaces in visible and near-infrared wavelengths [12, 13]. Here it should be mentioned that even though the conversion efficiency has been increased, it is still inferior to the dielectric metasurface platforms [17, 18]. Although the *PCR* drops to ~35% at the short wavelength of $\lambda = 775$ nm, the fabricated metasurface sustains the good performance of generating a focused vortex beam with linear-polarization conversion (Supplementary Figure S4). Subsequently, we measured the absolute focusing efficiency of the total reflected beam and the cross-polarized component (Figure 4E). Predictably, the vortex beam is predominantly focused in cross-polarization with the averaged efficiency exceeding 27%, exhibiting at least 10-fold enhancement compared with that from V-shaped antennas [12], while the remaining co-polarized component is strongly suppressed over the wavelength range from 800 to 950 nm. At the design wavelength of $\lambda_d = 850$ nm, the measured focusing efficiency of the polarization-converted vortex beam is found to be ~26%, which is considerably lower than the averaged cross-polarized reflectivity of the four meta-atoms (~85%). We believe that the discrepancies are related to the imperfections and the surface roughness of the fabricated sample, the slight variations in the optical constants of the deposited Au, the increased damping related to the titanium adhesion layer between the Au and SiO_2 layers, different excitation conditions in the simulation and experiment, and the near-field coupling between adjacent meta-atoms that is not considered in the simulations [27]. As a final comment, it should be emphasized that the focused vortex-beam generator shows the similar performance of orthogonal linear-polarization conversion and vortex-beam focusing when the incident polarization is switched to *y*-polarization, in accord with the symmetry of the meta-atoms (Supplementary Figure S5).

In addition to the aforementioned single-focal metasurfaces capable of generating focused vortex beams in cross-polarization with different topological charges, we further extended our approach to realize a dual-focal metasurface that transforms the incident Gaussian beam into two slightly focused spots with distinct wavefronts while maintaining the capability of orthogonal linear-polarization conversion. In our design, the dual-focal metasurface is segmented into two sub-metasurfaces, which spatially focus a linearly polarized incident beam to an orthogonal-polarized beam and a vortex beam with intensity singularity, respectively, at different locations in the same focal plane. Therefore, the dual-focal metasurface should impose different phase profiles on the left and right to convert the incident planar wavefronts into two spherical wavefronts in reflection:

$$\varphi(x, y) = \begin{cases} \dfrac{2\pi}{\lambda_d}\left(\sqrt{\left(x+\dfrac{s}{2}\right)^2 + y^2 + f^2} - \sqrt{\left(\dfrac{s}{2}\right)^2 + f^2}\right) & (x \ll 0) \\ \dfrac{2\pi}{\lambda_d}\left(\sqrt{\left(x-\dfrac{s}{2}\right)^2 + y^2 + f^2} - \sqrt{\left(\dfrac{s}{2}\right)^2 + f^2}\right) + l \cdot \arctan\left(\dfrac{y}{x-\dfrac{s}{2}}\right) & (x > 0) \end{cases} \quad (2)$$

where λ_d is the wavelength in free space, f is the focal length along the axial direction, l is the topological charge, and s is the distance between two foci. Figure 5A plots the phase profile of the dual-focal metasurface with a diameter of $D = 50$ μm, a focal length of $f = 60$ μm, the topological charge of $l = 1$, and the separation between the two foci of $s = 20$ μm. Similarly, the corresponding meta-atoms are properly selected and arranged with a uniform rotation of 45° with respect to the *x*-axis after discretizing the phase distribution on the *x*–*y* grid, as shown in Figure 5B. Figure 5C presents the SEM image of the fabricated dual-focal metasurface, where the spiral pattern can be clearly seen on the right side. Subsequently, the dual-focal sample was measured using the same setup, and the intensity distributions at the corresponding focal planes of different wavelengths are displayed in Figure 5D–I. Generally, two focal spots are formed with negligible backgrounds, indicating the excellent phase realization. The diffraction-limited focal spot on the left has a Gaussian-distributed intensity profile, while the right spot exhibits the intensity singularity with a minimum in the central part. When a linear polarizer oriented 90° with respect to the illumination polarization was placed in front of the CCD camera to filter out any co-polarized light, the intensity profiles remain largely unaffected and the moderate noise is removed, qualifiedly indicating the high performance of our metasurface design. Here, the non-negligible noise is most likely associated with the imperfections in fabrication and the gap between two sub-metasurfaces, leading to increased co-polarized reflection.

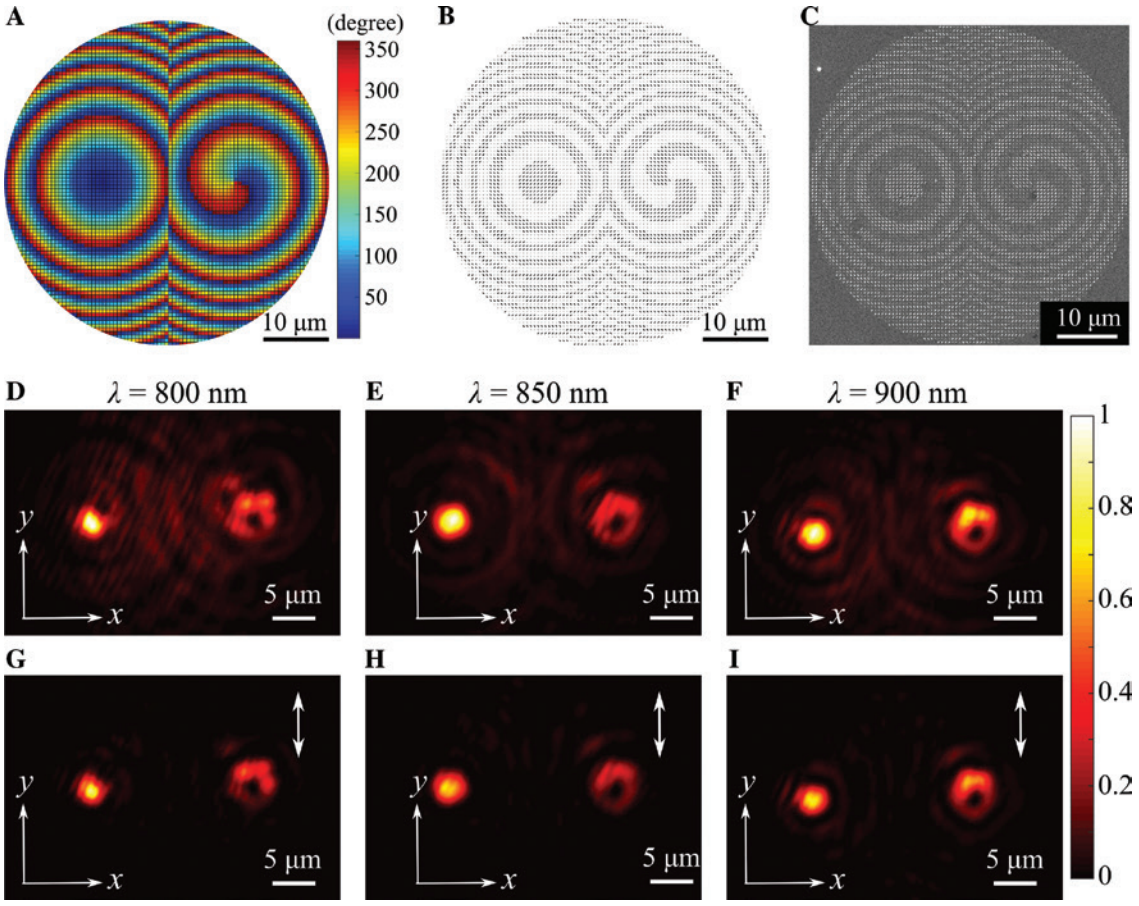

Figure 5: Design, fabrication, and experimental demonstration of the dual-focal metasurface.
(A) Calculated phase profile, (B) designed pattern, and (C) SEM image of the dual-focal metasurface that simultaneously generates dual-focal spots with different intensity profiles for the cross-polarized reflected light, where the left sub-metasurface is to create the convention focused Gaussian beam and the right sub-metasurface is responsible for generating a focused vortex beam. The dual-focal metasurface has a diameter of $D = 50$ μm, a focal length of $f = 60$ μm, the topological charge of $l = 1$, and the distance between two foci of $s = 20$ μm. (D–F) Measured intensity profiles at the corresponding focal planes of different wavelengths without polarization analyzer. (G–I) Measured intensity profiles at the corresponding focal planes of different wavelengths when a linear polarizer oriented 90° with respect to the illumination polarization was placed in front of the camera. In (D–I), an *x*-polarized Gaussian beam is impinging on the sample at normal incidence.

3 Conclusions

In this work, we have utilized GSP metasurfaces to realize efficient orthogonal linear-polarization conversion and focused vortex-beam generation simultaneously, mimicking thereby the functionalities of conventional HWPs, lenses, and q-plates. The fabricated metasurface sample exhibits the excellent capability of orthogonal linear-polarization conversion and focused vortex-beam generation within the wavelength range of 800–950 nm with an averaged polarization conversion ratio of ~80% and absolute focusing efficiency exceeding 27% under normal illumination with the *x*-polarized beam. Importantly, this approach has been extended to realize a dual-focal metasurface with distinctly engineered intensity profiles by using segmented metasurfaces, where an orthogonal-polarized beam with Gaussian-distributed intensity and a vortex-beam with intensity singularity have been experimentally implemented. Owing to the compactness and remarkable multifunctional performance, such metasurfaces enable easy integration with the existing photonic technology and sophisticated application in plasmonic and photonic circuits and systems [28–31].

Acknowledgments: This work was funded by the European Research Council (Grant 341054, Funder Id: http://dx.doi.org/10.13039/100011199), the University of Southern Denmark (SDU2020 funding, Funder Id: http://dx.doi.org/10.13039/501100006356), and VKR Foundation (Award in Technical and Natural Sciences 2019

and Grant No. 00022988, Funder Id: http://dx.doi.org/10.13039/100008398). FD would like to thank Yun Ding for help during the optical characterization.

References

[1] Allen L, Beijersbergen MW, Spreeuw RJ, Woerdman JP. Orbital angular momentum of light and the transformation of Laguerre-Gaussian laser modes. Phys Rev A 1992;45:8185–9.
[2] Yao AM, Padgett MJ. Orbital angular momentum: origins, behavior and applications. Adv Opt Photon 2011;3:161–204.
[3] Wang J, Yang J, Fazal IM, et al. Terabit free-space data transmission employing orbital angular momentum multiplexing. Nat Photon 2012;6:488–96.
[4] Ng J, Lin ZF, Chan CT. Theory of optical trapping by an optical vortex beam. Phys Rev Lett 2010;104:103601.
[5] D'Ambrosio V, Nagali E, Walborn SP, et al. Complete experimental toolbox for alignment-free quantum communication. Nat Commun 2012;3:961.
[6] Kildishev AV, Boltasseva A, Shalaev VM. Planar photonics with metasurfaces. Science 2013;339:1232009.
[7] Yu N, Capasso F. Flat optics with designer metasurfaces. Nat Mater 2014;13:139–50.
[8] Chen HT, Taylor AJ, Yu N. A review of metasurfaces: physics and applications. Rep Prog Phys 2016;79:076401.
[9] Ding F, Pors A, Bozhevolnyi SI. Gradient metasurfaces: a review of fundamentals and applications. Rep Prog Phys 2018;81:026401.
[10] Kamali SM, Arbabi E, Arbabi A, Faraon A. A review of dielectric optical metasurfaces for wavefront control. Nanophotonics 2018;7:1041–68.
[11] Genevet P, Yu N, Aieta F, et al. Ultra-thin plasmonic optical vortex plate based on phase discontinuities. Appl Phys Lett 2012;100:013101.
[12] Karimi E, Schulz SA, Leon ID, et al. Generating optical orbital angular momentum at visible wavelengths using a plasmonic metasurface. Light Sci Appl 2014;3:e167.
[13] Pu M, Li X, Ma X, et al. Catenary optics for achromatic generation of perfect optical angular momentum. Sci Adv 2015;1:e1500396.
[14] Maguid E, Yulevich I, Veksler D, et al. Photonic spin-controlled multifunctional shared-aperture antenna array. Science 2016;352:1202–6.
[15] Devlin RC, Ambrosio A, Rubin NA, Mueller JP, Capasso F. Arbitrary spin-to-orbital angular momentum conversion of light. Science 2017;358:896–901.
[16] Heiden JT, Ding F, Linnet J, et al. Gap-surface plasmon metasurfaces for broadband circular-to-linear polarization conversion and vector vortex beam generation. Adv Opt Mater 2019;7:1801414.
[17] Yang Y, Wang W, Moitra P, et al. Dielectric meta-reflectarray for broadband linear polarization conversion and optical vortex generation. Nano Lett 2014;14:1394–9.
[18] Arbabi A, Horie Y, Bagheri M, Faraon A. Dielectric metasurfaces for complete control of phase and polarization with subwavelength spatial resolution and high transmission. Nat Nanotech 2015;10:937–43.
[19] Ma X, Pu M, Li X, et al. A planar chiral meta-surface for optical vortex generation and focusing. Sci Rep 2015;5:10365.
[20] Mehmood MQ, Mei S, Hussain S, et al. Visible-frequency metasurface for structuring and spatially multiplexing optical vortices. Adv Mater 2016;28:2533–9.
[21] Shi Z, Khorasaninejad M, Huang Y, et al. Single-layer metasurface with controllable multiwavelength functions. Nano Lett 2018;18:2420–7.
[22] Tang S, Li X, Pan W, et al. High-efficiency broadband vortex beam generator based on transmissive metasurface. Opt Express 2019;27:4281–91.
[23] Ding F, Yang Y, Deshpande R, Bozhevolnyi SI. A review of gap-surface plasmon metasurfaces: fundamentals and applications. Nanophotonics 2018;7:1129–56.
[24] Grady NK, Heyes JE, Chowdhury DR, et al. Terahertz metamaterials for linear polarization conversion and anomalous refraction. Science 2013;340:1304–7.
[25] Jiang SC, Xiong X, Hu YS, et al. Controlling the polarization state of light with a dispersion-free metastructure. Phys Rev X 2014;4:021026.
[26] Ding F, Wang Z, He S, Shalaev VM, Kildishev AV. Broadband high-efficiency half-wave plate: a supercell-based plasmonic metasurface approach. ACS Nano 2015;9:4111–9.
[27] Deshpande R, Zenin VA, Ding F, Mortensen NA, Bozhevolnyi SI. Direct characterization of near-field coupling in gap plasmon-based metasurfaces. Nano Lett 2018;18:6265–70.
[28] Cai T, Tang S, Wang G, et al. High-performance bifunctional metasurfaces in transmission and reflection geometries. Adv Opt Mater 2017;5:1600506.
[29] Ding F, Deshpande R, Bozhevolnyi SI. Bifunctional gap-plasmon metasurfaces for visible light: polarization-controlled unidirectional surface plasmon excitation and beam steering at normal incidence. Light Sci Appl 2018;7:17178.
[30] Tang S, Cai T, Xu HX, et al. Multifunctional metasurfaces based on the "merging" concepts and anisotropic single-structure meta-atoms. Appl Sci 2018;8:555.
[31] Hayenga W, Parto M, Ren J, et al. Direct generation of tunable orbital angular momentum beams in microring lasers with broadband exceptional points. ACS Photonics 2019;6:1895–901.

Supplementary Material: The online version of this article offers supplementary material (https://doi.org/10.1515/nanoph-2019-0235).